

## Hierarchical thermoelectrics

### Crystal grain boundaries as scalable phonon scatterers

Selli, Daniele; Boulfelfel, Salah Eddine; Schapotschnikow, PZ; Donadio, Davide; Leoni, Stefano

**DOI**

[10.1039/c5nr05279c](https://doi.org/10.1039/c5nr05279c)

**Publication date**

2016

**Document Version**

Final published version

**Published in**

Nanoscale

**Citation (APA)**

Selli, D., Boulfelfel, S. E., Schapotschnikow, PZ., Donadio, D., & Leoni, S. (2016). Hierarchical thermoelectrics: Crystal grain boundaries as scalable phonon scatterers. *Nanoscale*, 8(6), 3729-3738. <https://doi.org/10.1039/c5nr05279c>

**Important note**

To cite this publication, please use the final published version (if applicable). Please check the document version above.

**Copyright**

Other than for strictly personal use, it is not permitted to download, forward or distribute the text or part of it, without the consent of the author(s) and/or copyright holder(s), unless the work is under an open content license such as Creative Commons.

**Takedown policy**

Please contact us and provide details if you believe this document breaches copyrights. We will remove access to the work immediately and investigate your claim.



Cite this: *Nanoscale*, 2016, 8, 3729

## Hierarchical thermoelectrics: crystal grain boundaries as scalable phonon scatterers

Daniele Selli,<sup>a,b,c</sup> Salah Eddine Boulfefel,<sup>d</sup> Philipp Schapotschnikow,<sup>e,f</sup> Davide Donadio<sup>b,g</sup> and Stefano Leoni<sup>\*a,h</sup>

Thermoelectric materials are strategically valuable for sustainable development, as they allow for the generation of electrical energy from wasted heat. In recent years several strategies have demonstrated some efficiency in improving thermoelectric properties. Dopants affect carrier concentration, while thermal conductivity can be influenced by alloying and nanostructuring. Features at the nanoscale positively contribute to scattering phonons, however those with long mean free paths remain difficult to alter. Here we use the concept of hierarchical nano-grains to demonstrate thermal conductivity reduction in rocksalt lead chalcogenides. We demonstrate that grains can be obtained by taking advantage of the reconstructions along the phase transition path that connects the rocksalt structure to its high-pressure form. Since grain features naturally change as a function of size, they impact thermal conductivity over different length scales. To understand this effect we use a combination of advanced molecular dynamics techniques to engineer grains and to evaluate thermal conductivity in PbSe. By affecting grain morphologies only, *i.e.* at constant chemistry, two distinct effects emerge: the lattice thermal conductivity is significantly lowered with respect to the perfect crystal, and its temperature dependence is markedly suppressed. This is due to an increased scattering of low-frequency phonons by grain boundaries over different size scales. Along this line we propose a viable process to produce hierarchical thermoelectric materials by applying pressure *via* a mechanical load or a shockwave as a novel paradigm for material design.

Received 5th August 2015,  
Accepted 14th January 2016

DOI: 10.1039/c5nr05279c

www.rsc.org/nanoscale

## Introduction

Thermoelectrics are materials of top priority for waste heat conversion into valuable energy.<sup>1–5</sup> The family of narrow gap semiconducting lead chalcogenides PbX (X = S, Se, Te) with a rocksalt crystal structure is attracting considerable attention for energy conversion applications.<sup>6,7</sup> The efficiency of a material in thermoelectric conversion is related to and limited by its dimensionless figure of merit  $ZT = \sigma S^2 T / \kappa$ . In this

expression,  $\sigma$  is the electrical conductivity,  $S$  is the Seebeck coefficient,  $T$  is the absolute temperature, and  $\kappa = \kappa_e + \kappa_l$  accounts for the total thermal conductivity, which is the sum of an electronic (e) and a lattice (l) contribution. An improved figure of merit is achieved, for example, by introducing dopants. The introduction of Na for instance affects carrier concentration and at the same time lowers lattice thermal conductivity *via* the formation of Na-rich nano-precipitates<sup>8</sup> and Na doped polycrystalline PbSe.<sup>9</sup> Other approaches based on spinodal decomposition, nucleation and growth have been successfully used to prepare materials with very low lattice thermal conductivity,<sup>10</sup> which are not solid solutions but heterogeneous at the nanoscale. The critical issue therein is the controlled production of coherent nanoscale precipitates for more efficient phonon scattering.<sup>11</sup> While in general it represents a powerful paradigm for better thermoelectric compounds, nanostructuring can affect only portions of the phonon spectrum, *i.e.* roughly those modes with mean free paths with similar length scales as the nanostructures. In diamond, silicon and SiGe alloys, the relevant mean free paths for heat carriers extend over at least three orders of magnitude.<sup>12–17</sup> Therein, nanograins can act as phonon scatterers. In PbSe this distribution is narrower and implies

<sup>a</sup>Cardiff University, School of Chemistry, Park Place, CF10 3AT Cardiff, UK

<sup>b</sup>Max Planck Institute for Polymer Research, Ackermannweg 10, 55128 Mainz, Germany

<sup>c</sup>Technische Universität Dresden, Institut für Theoretische Chemie, 01062 Dresden, Germany

<sup>d</sup>Georgia Institute of Technology, School of Chemical & Biomolecular Engineering, Atlanta, GA 30332-0100, USA

<sup>e</sup>Process and Energy Laboratory, Delft University of Technology, Delft, 2628 CA, The Netherlands

<sup>f</sup>Brains for Hire, Valpichlerstr. 86, 80686 Munich, Germany

<sup>g</sup>Department of Chemistry, University of California Davis, One Shields Ave., Davis, CA 95616, USA

<sup>h</sup>University of Berne, Department of Chemistry and Biochemistry, Freiestrasse 3, 3012 Bern, Switzerland. E-mail: leonis@cf.ac.uk



shorter mean free paths, up to 100 nm, according to first-principles calculations.<sup>18</sup> Therefore a different approach to structuring this material is required, if the whole range of main heat carriers has to be affected: one in which nanostructuring represents only one scale of an otherwise hierarchical distribution of lengths. Material engineering at the meso-scale is emerging as a more efficient strategy of controlling phonon scattering, where also medium to long mean free paths are affected. This strategy requires complete understanding of material morphology and its consequences for the thermal conductivity at varying length scales. Pioneering work in this direction has been recently performed for the SrTe–PbTe system with Na doping<sup>19</sup> and MgTe–PbTe.<sup>20</sup> Therein, besides nanoscale precipitates, grains up to the micrometer scale present a novel ingredient. The presence of grains and grain boundaries is understood to be a means to trespass the *ZT* threshold of 2. As a result, grains and domain boundaries open novel perspectives in material engineering,<sup>21–23</sup> for they implement a natural way of size re-scaling over different lengths.<sup>24</sup> In contrast to the local nano-precipitates, grains and their boundaries offer a way of accommodating disparate scale lengths in a material, without necessarily affecting composition. While they can be used together with doping and nanoscale precipitates as proven in experiments,<sup>19</sup> grains should be capable of lowering thermal conductivity on their own, at “constant chemistry” so to speak.

Guided by this idea, in this work we investigate the formation and thermal conductivity of polycrystalline PbSe, with grains of increasing hierarchical sizes, in order to understand and systematise the impact of morphology on heat transport. The formation of grains and boundaries typically accompanies solid–solid reactions and structural phase transitions in general. Exploiting the polymorphism of PbSe, which, from the ground-state structure rocksalt (B1), transforms into the CsCl type structure (B2) under pressure and back to B1 on releasing it, it is possible to obtain a range of metastable PbSe rocksalt structures, which contain grains bounded into domains. On varying the size of the simulated system, grain features as seen in real materials can be produced and studied in detail. While this is a useful and handy approach to modelling domains without cumbersome *a priori* assumptions, this step provides at the same time a direct link to its experimental realisation, based on mechanical loads or milling approaches.<sup>3,25</sup> This way one can directly shape an eventual experimental process utilising our results and methods.

To understand how grains and grain boundaries form in PbSe, we first investigated the mechanism of the B1–B2 structural phase transition in PbSe using transition path sampling (TPS) molecular dynamics (MD).<sup>26,27</sup> The transformation path crosses an intermediate, metastable configuration of a roughly B33 type structure (CrB/III).<sup>28</sup> When pressure is released this intermediate transforms into B1. This transformation is accompanied by the formation of grains.

Subsequently, the thermal conductivity is calculated for grain-free PbSe, and for several B1 structures containing grains

with varying size. This is done using equilibrium molecular dynamics, from which thermal lattice conductivity can be derived *via* computation of the thermal flux.<sup>29</sup> Finally, the impact of grains on phonon mean free paths is evaluated and compared to grain-free PbSe. Discussion of the findings concludes the paper.

## Results

### B1–B2 phase transition in PbSe

PbSe crystallises in the rocksalt (B1) type structure of space group symmetry  $Fm\bar{3}m$ . In the pressure range 9–16 GPa,<sup>28,30–33</sup> PbSe transforms into the CsCl (B2) type; the phase transition involves metallisation (B2 is metallic). Several studies have concentrated on the prediction and detection of intermediate metastable configurations along the transformation path from B1 to B2.<sup>28,30–33</sup> Phases of  $Pnma$  (GeS type structure, B16) and  $Cmcm$  (CrB type structure, B33) symmetries are possible intermediates along the paths. For PbSe, accurate transport and X-ray diffraction studies under pressure identify an intermediate phase of the CrB type structure at around 9.5 GPa,<sup>31</sup> which is in agreement with theoretical predictions.<sup>33</sup>

The assessment of a structural phase transition mechanism, including possible intermediates, can be approached with different strategies. The main methods make use of extended Landau theory in combination with first principles calculations,<sup>34</sup> metadynamics,<sup>35,36</sup> and, as the method of choice here, molecular dynamics (MD) simulations based on the Transition path sampling scheme, TPS (see the Methods section for details). This approach has been successfully used to elucidate mechanisms of several ionic (B1–B2) phase transitions, as well as other compounds and chemical elements.<sup>27,37–39</sup> It yields very detailed transformation mechanisms as it does not artificially enforce any collective transformation. As NaCl and PbSe both transform into B2 under pressure, some of the previous experiences accumulated on the B1–B2 polymorphism are advantageously used here.<sup>40</sup> The MD-TPS method works iteratively on a so-called first trajectory (initial path), which connects B1 to B2. The process of elucidating the true mechanism consists in repeatedly perturbing the initial path, within a Monte Carlo scheme, until the calculation is converged to the optimal path, biased by its importance. While the initial mechanism is typically concerted and collective, as it is derived from a general scheme of interpolating the intermediate configuration between two limiting structures, for instance B1 and B2 (see the Methods section for details), the converged regime is characterised by nucleation and growth. Furthermore, intermediate configurations can be visited along the path of the transformation, which can be transient configurations or appropriate metastable phases. The transition pressure for the pair potential used here is 12 GPa,<sup>41</sup> which is within the experimental range.<sup>28,30–33</sup> Pressure itself and the reconstructive character of the B1–B2 transition can generate grains, like those demonstrated for CdSe.<sup>27</sup> We do not have direct experimental evidence of domain



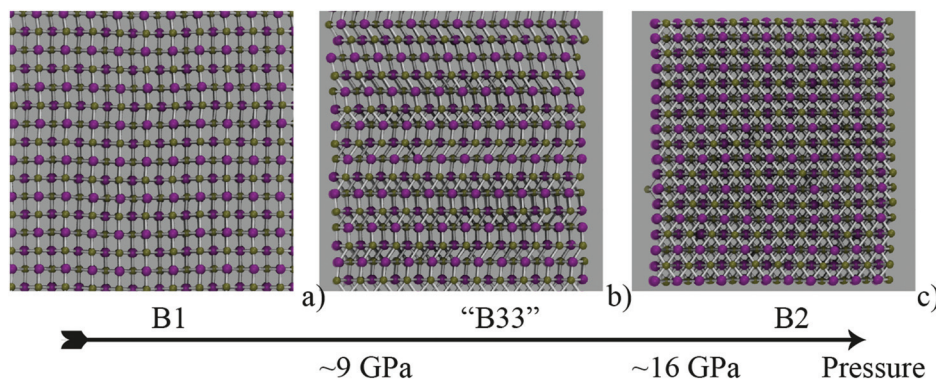


**Fig. 1** Representative path of structural transformation from B1 to B2 in PbSe. TPS MD calculations identify an intermediate with B33 structural features, showing the typical alternation of triangular and square layers along [010]. The latter can be stabilised in the lower pressure range, while higher pressure favours B2. Several simulations were performed in the range 9–16 GPa, at 300 K, with a box of 1980 PbSe pairs.

morphologies in PbSe, which would allow for a comparison of features. Nonetheless, since the same concept of overall transformation pathway convergence also includes an *optimisation of the final B1 product*, we trust that we are reliably representing the B1 phase after phase transformation, characterised by grain features.

The initial B1–B2 path in PbSe was modelled similarly to how it was done for NaCl,<sup>40</sup> which also crystallises in the same type structures and bears many common aspects with respect to its polymorphism.<sup>34</sup> The aim of this modelling step is to obtain a first trajectory (see the Methods section for further details). The initial trajectory was iterated in MD-TPS until the mechanistic regime had converged, *i.e.* no departures from a particular mechanism were detectable. Three snapshots of representative initial, intermediate and final configurations are shown in Fig. 1a–c, respectively. To monitor the evolution of the calculations and of the transition, a suitable order parameter is necessary. Given the compact nature of the structures, a good choice is the first coordination sphere (fCN), which is 6 in B1 and becomes 8 in B2. To precisely identify any intermediate step, the second and third coordination spheres (sCN, tCN) were also considered.<sup>42</sup> In Fig. 2 the progress of the three CNs is monitored as a function of the progress of the transition. Three horizontal dotted lines mark the values of the CNs, which amount to 7–22–47 for the B33 type.

The three CNs cross the threshold values for B33 quasi-synchronously, indicating that the transition is visiting an intermediate of B33 characteristics (configuration in Fig. 1b). The typical pattern of B33 is apparent (alternating square and triangular patterned layers), some parts are not fully locked-in to this pattern though. However, on average the B33 emerges as an intermediate, and can be quenched at lower pressure (~6–9 GPa, at which B2 would not form), in accordance with experimental indications. From TPS finite temperature molecular dynamics simulations, the intermediate role of configurations related to B33 is thus confirmed, in the context of nucleation and growth of extended interfaces between regions of B1, B33 and B2 structures.

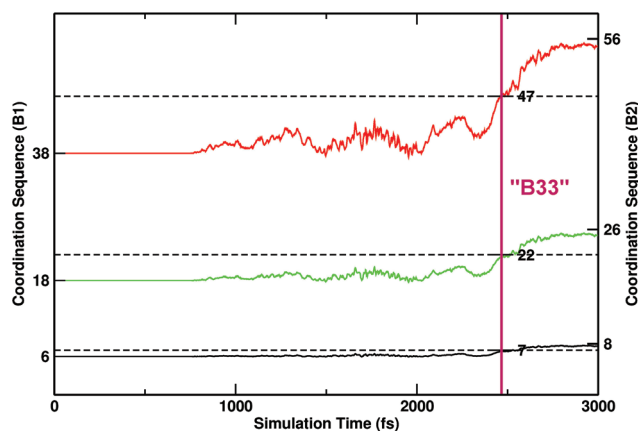


**Fig. 2** Progression of coordination sequences (CNs) calculated along the time coordinate for transformation trajectories in the convergence regime. Three levels of coordination spheres are considered. The numbers indicated on the left and right side correspond to B1 and B2, respectively. CN values that are characteristic for the B33 structure are also indicated in the graph. The evolution of the three coordination shows a simultaneous plateau marked with a vertical magenta line, which corresponds to B33.

### Grains and grain boundaries

The elucidation of the B1–B2 phase transition is the starting point for the construction of realistic PbSe structures with grains. Here realistic means that the grains are calculated from a particular simulation protocol, without prior knowledge or assumptions on their geometries. For this, intermediate configurations like the one of Fig. 1b are used as the starting point of further molecular dynamics calculations at normal conditions. The metastable nature of such intermediate configurations causes them to transform back into the ground state, B1. This takes place in a non-collective way though, having different regions transforming into B1 at different times and along different crystallographic directions, such that the process yields B1 PbSe with distinguishable coherent B1





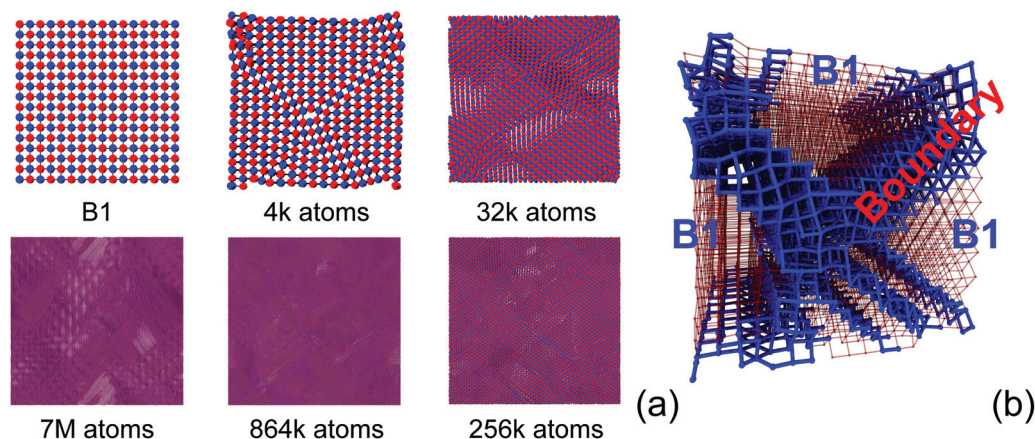


**Fig. 3** (a) Morphologies of B1 grain boundaries obtained from supercell magnification of the B33 intermediate of Fig. 1 (original cell (4k, 3960 atoms),  $2 \times 2 \times 2$  (32k, 31 680 atoms),  $4 \times 4 \times 4$  (256k, 253 444 atoms),  $6 \times 6 \times 6$  (864k, 855 360 atoms) and  $12 \times 12 \times 12$  (7M, 6 842 880 atoms)), after NpT-MD calculations. (b) Detailed representation of the smallest grain obtained (4k): regions of the coherent B1 structure are separated by B1 grain boundaries. A strong anisotropy can be noticed, as B1 percolates in one direction only (red framework), normal to the plane. The structural motif of the boundaries resembles the NiAs type structure (blue regions). Pb and Se are not differentiated to emphasise structural features.

zones, which are separated into grains by grain boundaries. The relaxation of the 3960 atom cell yields boundaries along two directions only. Systematically doubling the edges of the box yields more complex grain geometries, which are increasingly isotropic, *i.e.* none of the grains is a perfect B1 beyond a certain length (Fig. 3a). The process of enlarging the box and the resulting PbSe grain structures are shown in Fig. 3. The still rather anisotropic structure resulting from the 3960 atom box, which contains coherent and percolating B1 domains in a distinct direction ( $z$  axis), is shown in Fig. 3b.

### Thermal transport in PbSe and role of grains

The effect of grains and grain boundaries on pure PbSe can be appreciated already at the lowest step of magnification. The evaluation of  $\kappa_1$  as a function of temperature for grain-free PbSe and for the smallest PbSe box containing grains (3960 atom box) is shown in Fig. 4. The use of classical molecular dynamics for PbSe at room and higher temperatures is justified, since the Debye temperature of PbSe does not exceed 200 K.<sup>43</sup> For single crystalline PbSe the thermal conductivity decays as the inverse of the temperature, dropping from 2.4 W mK<sup>-1</sup> at 300 K to  $\sim 1.12$  at 700 K as in experiments,<sup>44</sup> since anharmonicity is the only source of scattering. Our estimate of  $\kappa_1$  over the whole temperature range is in good agreement with former first-principles calculations.<sup>18</sup>

For anisotropic systems containing grains,  $\kappa_1$  is resolved for each Cartesian component. Anisotropy strongly impacts thermal conductivity. While there is an overall dropping of  $\kappa_1$  with respect to grain-free PbSe, the  $z$  component  $\kappa_{1,z}$  is only partially affected. By inspection of Fig. 3b, the PbSe grains are coherently aligned and percolate along  $z$ . In turn  $\kappa_{1,z}$  diminishes as a function of temperature, yet to a lesser extent with respect to grain-free PbSe. The other two components  $\kappa_{1,x}$  and  $\kappa_{1,y}$  show different behaviour. Any structural path along  $x$  and  $y$  crosses grain boundaries. Both  $\kappa_{1,x}$  and  $\kappa_{1,y}$  have low

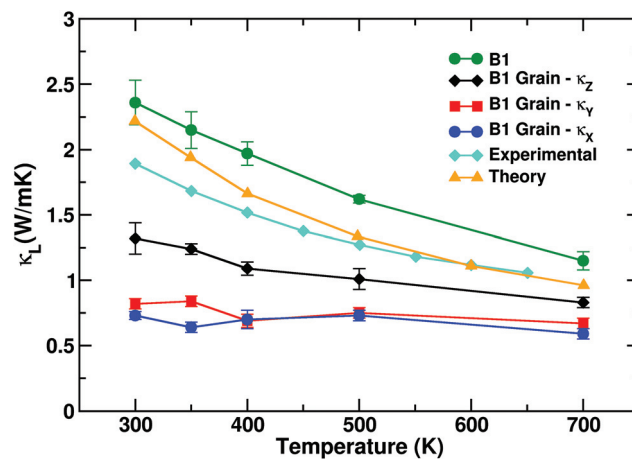


**Fig. 4** Evolution of  $\kappa_1$  as a function of temperature for feature-free PbSe, compared to the 3960 atom system of Fig. 3b.  $\kappa_1$  for the latter is resolved in its Cartesian components;  $\kappa_{1,z}$  displays lattice thermal conductivity values larger than  $\kappa_{1,x}$  and  $\kappa_{1,y}$ , which are the directions along which grain boundaries are crossed. The overall thermal conductivity is notably reduced with respect to pure B1, as well as the temperature dependence is nearly lost. Size effect corrections have been included. Experimental data are taken from ref. 8, Fig. 3a. Comparison with theory is based on *ab initio* data from ref. 18.

values around  $\sim 0.7$  W mK<sup>-1</sup> at 300 K (for the impact of the size effect on absolute thermal conductivity values, see below). Similar to what is observed in silicon nanomeshes,<sup>45</sup> percolation of grains along a periodic direction leads to anisotropic thermal conduction, thus suggesting that structuring in grains can be used to finely tune the thermal conductivity of PbSe. The dependence on the temperature is appreciably reduced, showing a similar response over the whole temperature range considered, 300–700 K. Grains thus affect thermal conductivity both in terms of a reduction of  $\kappa_1$  and flattening the dependence of  $\kappa_1$  on temperature.



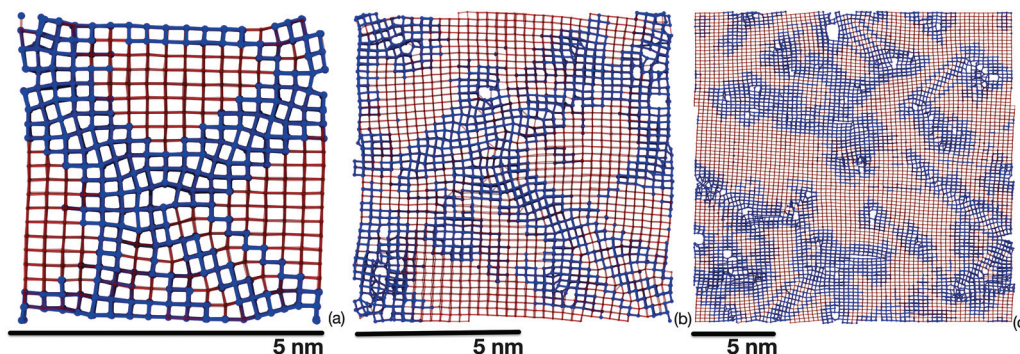


**Fig. 5** Grain size distributions for 4k, 32k and 256k atom systems. Regions of the coherent B1 structure of increasing size are separated by grain boundaries. Using the black bar below each snapshot as the reference length (5 nm), the largest grain size in (a) is around 3 nm, in (b) it is in the order of 5 nm, while in (c) grains as large as 15 nm can be observed. Importantly, sizes typical of the previous cell size are still contained in the larger, subsequent one. B1 grains are red coloured, while grain boundaries are blue. Contrary to grain size, grain boundary widths do not grow noticeably larger, comprising 5 layers on average. The distinction between coherent B1 regions and boundaries is based on the coordination sequence.<sup>42</sup>

### Thermal conductivity of PbSe with extensive grain features

In this section we assess the role of the distribution of grain size on lowering thermal conductivity. Systems comprising 4k, 32k and 256k atoms, as displayed in Fig. 3a were considered. Their sizes span two orders of magnitude, and the grain features in the larger boxes affect all three Cartesian directions in an increasingly isotropic manner. A typical size distribution is shown in Fig. 5. Grain sizes in the smallest (4k) cell are around 3 nm wide, 5 nm in the 32k one, and up to 15 nm in the largest 256k atom cell considered. Noticeable is the distribution of grain sizes as the system is rescaled: grain sizes characteristic of a smaller system are preserved in the subsequent, larger systems. To quantitatively capture this effect, the 4k and 32k systems were enlarged by replication, to match the size of the 256k system. The coordinates of all these three systems were Fourier transformed, considering Pb atoms only, for simplicity. In Fig. 6 the peak intensities are plotted as a function of the  $hkl$  vector magnitude,  $||hkl||$ .  $hkl$  Triplets (Miller indices) describe planes in crystals, and sensibly reflect (changed) atomic arrangements. For the small 4k system, the intensity is accumulated around one main peak. For the 32k system, additional peaks appear mainly at lower  $hkl$ , signalling longer distances between planes and hence larger domains. This trend is even more pronounced in the 256k system, where peak clustering is clearly visible. Therein, the rescaling of sizes is apparent if a series of  $hkl$  are considered (Fig. 6, inset), like for example  $h = [30-40]$ ,  $k = [0, 1, 2, 3, 4, \dots]$ ,  $l = 40$ , and the “cubic” permutations thereof. The centres of the cluster regions can be matched by such a series, which nicely illustrates the progressive and hierarchical growth of domains as a function of size.

We computed  $\kappa_1$  by equilibrium molecular dynamics as described in the Methods section. However, comparing thermal conductivity over disparate scales can be flawed due to size effects. For instance, small simulation boxes lead to an underestimation of  $\kappa_1$  due to the poor sampling of the low fre-

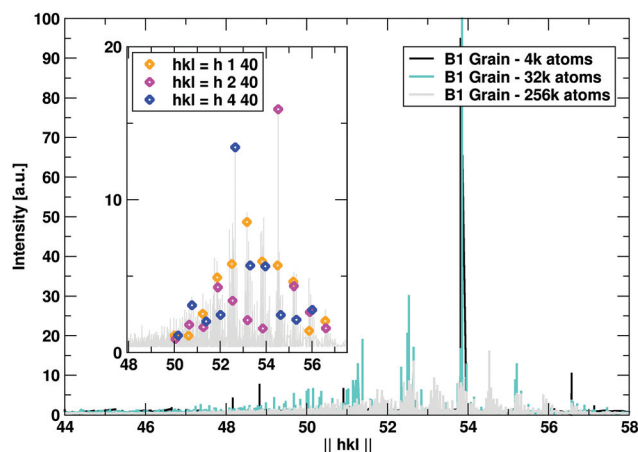


**Fig. 6** Fourier transformation of the 4k, 32k and 256k atom systems of Fig. 5, only Pb positions were considered for simplicity. Main plot:  $hkl$  values were chosen in the range  $[-40-40]$  in each direction. A peak clustering is apparent as a function of the number of atoms in the system, while domain size increases (shorter  $hkl$  vector modules,  $||hkl||$ ). Inset: Fourier peaks of the 256k atom system. Their sequence is matched by series of  $hkl$  vectors like indicated,  $30 \leq h \leq 40$ .

quency phonon branches. To correct for this effect, for each size,  $\kappa_1$  was rescaled to the value of  $\kappa_1$  of a corresponding system of the same size (see the Methods section for details). For a small system of 4k atoms the difference amounts to 0.3  $\text{W mK}^{-1}$ . In a 32k atom system it is reduced to less than 0.03  $\text{W mK}^{-1}$ , while for 256k atoms the numerical values converge.

Thermal conductivities as a function of size and temperature are shown in Fig. 7. The three sizes are distinguished by different colours. The general trend is one of continuous decrease of thermal conductivity towards a lower limit of approximately 0.72  $\text{W mK}^{-1}$  for the largest system considered, at 300 K. The impact of the different distribution of grain sizes is reflected on progressive curve flattening and downshifting,





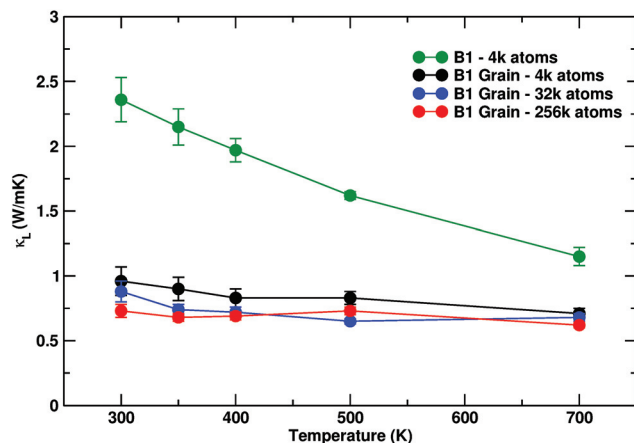


**Fig. 7** Thermal conductivity  $\kappa_L$  calculated as a function of temperature for pure B1 and B1 with grains (3960 atoms black, 31 680 blue and 253 444 red). Enlarging the system causes a marked reduction of lattice thermal conductivity as well as a lowered dependence on temperature, which is nearly lost for the 256k atoms grain, which shows a flat (red) line. Size effect corrections have been included. For the 3960 atom system Cartesian components have been averaged.

which is less pronounced but still appreciable as the cell size is increased. Furthermore, the anisotropy of  $\kappa_L$  observed in the 4k system vanished. While we expect a further lowering of the absolute value of  $\kappa_L$  by further increasing size, only fractional corrections of the top-scoring value for the 256k atoms grain can be expected. Even more than the achievement of the lowest  $\kappa_L$  values, it is worth noting the vanishing dependence of  $\kappa_L$  on temperature, which indicates that all the relevant heat carriers undergo significant grain boundary scattering.

### Lifetimes, group velocities and size effects

A detailed understanding of the impact of grains on phonon scattering is gained from evaluating phonon lifetimes and group velocities (see the Methods section). Alloys and nanoparticle embedding typically influence short-to-mid wavelength phonons, while lower frequencies are more difficult to affect in a systematic way.<sup>17,46</sup> In the previous section we have

shown that lattice thermal conductivity decreases as the distribution of the size of grains gets broader and their morphology more complex, as a consequence of hierarchical nanostructuring. Since allocation of the dynamic matrix  $\Omega$  rapidly limits the maximal attainable system size, the largest systems presented in the previous section could not be studied in such detail. To reproduce a similar size progression through two orders of magnitude, systems of 576, 3960, 11 520 atoms were prepared. The structures considered are shown in Fig. 8. The 576 and 3960 exhibit percolating grains in a periodic direction ( $z$ ) and therefore  $\kappa_L$  anisotropy. As previously discussed, using larger simulation boxes causes grain structuring over several length scales. Smaller systems show rather sharp, regular boundaries between differently oriented regions of the B1 structure. The 3960 atom system displays domain boundaries which are mirror planes (coherent grain boundaries), while the largest system considered in this section – 11 520 atoms – contains irregular grains of general orientation (incoherent grain boundaries) with a broader size distribution. This geometric variety implies pronounced differences in lifetimes and group velocities. Fig. 9(a–c) present a comparison among the group velocities and the lifetimes of these three systems and of a B1 crystal.

We show results for phonons in the frequency range up to 4 THz, which provide the main contribution to  $\kappa_L$ . This range of frequencies encompasses all the acoustic branches and the lowest optical branches of the B1 structure. The  $x$  component of the group velocities as a function of frequency, calculated on mesh  $q$ -points along the  $\Gamma$ - $X$  direction is reported in Fig. 9(a). The plot shows the group velocities of the two degenerate TA modes and the LA mode (black dots) of the pristine B1 crystal. Their value is in good agreement with the *ab initio* calculations by Tian *et al.*<sup>18</sup> In turn, we must point out that the optical modes with our empirical potential reach up to about 7 THz (not shown), thus exceeding the *ab initio* frequency range. Such a difference may also affect the scattering rates, thus leading to small discrepancies in the lifetimes of acoustic modes.

The presence of grains deeply affects the group velocities: we observe a softening of the acoustic modes at low frequency

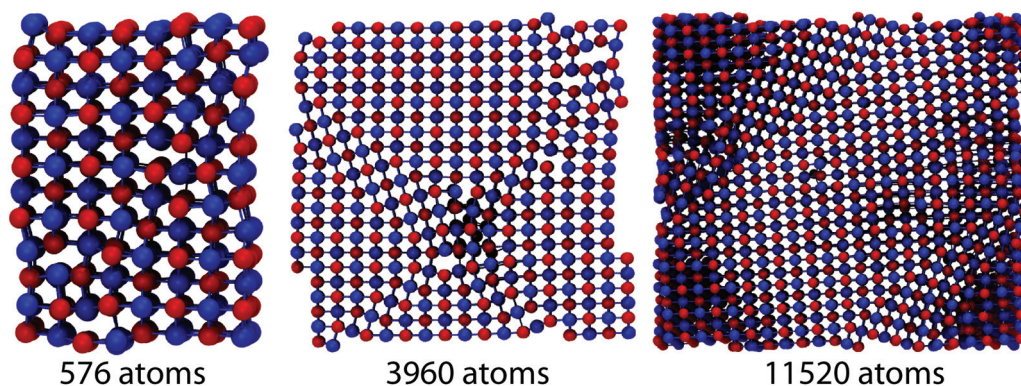


**Fig. 8** PbSe systems with grain features, considered for further calculations. Simulation box sizes comprise 576, 3960 and 11 520 atoms, respectively. Complexity of grain features evolves from smooth interfaces, to rough grains as system size increases.



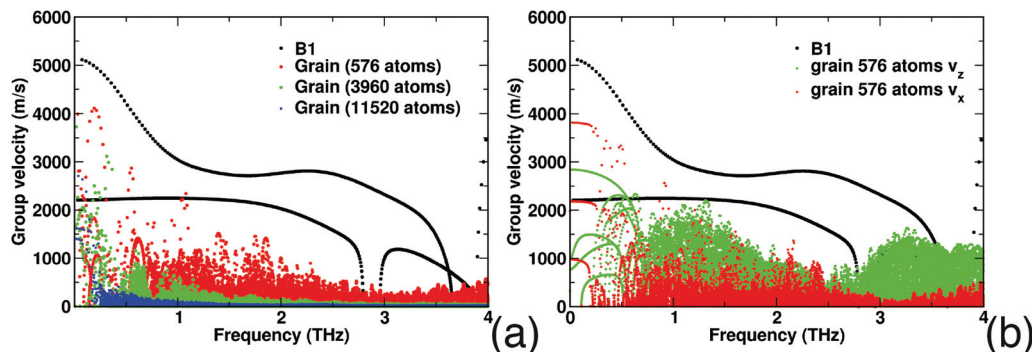


Fig. 9 Group velocities of vibrational modes as a function of frequency for (a) pure B1 and B1 with grains (576, 3960 and 11 520 atoms – red, green and blue, respectively). As grain features become more complex, lower frequencies are influenced, where group velocities soften.

that becomes more important the larger the size of the grains, suggesting a softer mechanical response of the larger hierarchical structures. In addition the systems of 3960 and 11 520 atoms exhibit vanishing group velocities beyond a decreasing frequency threshold of  $\sim 1.5$  and  $\sim 0.8$  THz, indicating flattening of the dispersion relations and the non-conducting character of the vibrational modes. Although the contribution to heat transport from phonons beyond this threshold is drastically reduced and mean free paths cannot be defined, these modes can still conduct heat through the “diffusion” mechanism proposed for amorphous silicon by Allen and Feldman.<sup>47</sup> In amorphous silicon this alternative mechanism accounts for about half the total  $\kappa_1$ .<sup>48</sup>

Fig. 9(b) provides a comparison of the  $x$  and  $z$  components of the group velocities in an anisotropic structure, with grain boundaries breaking only the  $xy$  plane. This structure displays anisotropic thermal conductivity, similar to the one showcased in Fig. 4. The figure shows the anisotropy in the group velocities: on the one hand acoustic modes at low frequency have smaller group velocities for propagating in the  $xy$  plane than along  $z$ . On the other hand for frequencies larger than 0.7 THz, group velocities are much larger for propagation in the  $z$  direction, thus leading to an overall larger  $\kappa_1$ .

Finally, Fig. 10 shows the effect of hierarchical structuring on phonon lifetimes. In the low frequency range ( $< 1$  THz) the dependence of lifetimes on frequency for pure B1 is  $\tau \propto \omega^{-2}$  (Fig. 10, blue), as expected for a crystalline solid, in which three-phonon scattering dominates. The lifetimes of the acoustic modes are in the same range as those computed by Tian *et al.*<sup>18</sup> e.g. at 0.2 THz  $\tau \sim 10^2$  ps. The lifetimes of the acoustic modes are largely reduced by the presence of grain boundaries. In the region between 1 and 3 THz the dependence of  $\tau$  on frequency is substantially flat, with values below 5 ps, and the larger system exhibiting slightly lower values than the smaller. While extended grain features (11 520 atoms grain) more pronouncedly affect the lowest optical frequency range from 3 to 4 THz, there is less of a strong signature of hierarchical grain features on lifetimes, compared to phonon group velocities.

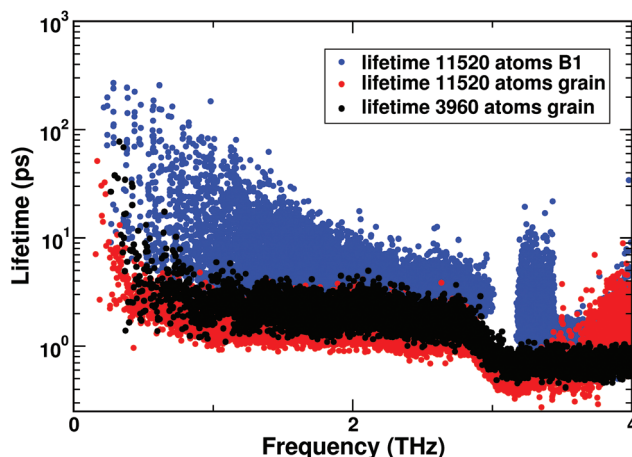


Fig. 10 Lifetimes of the vibrational modes for pure B1, compared with grains of 3960 and 11 520 atoms.

The observed major reduction of phonon group velocities, supplemented by a less dramatic reduction of lifetimes, leads to the systematic decrease of thermal conductivities in polycrystalline PbSe. A broad distribution of grain sizes is essential to lower the contribution to  $\kappa_1$  across the whole spectrum of relevant frequencies, including modes in the order of 0.5 THz and below. The overall reduction  $\kappa_1$  is however limited by the occurrence of non-propagative mechanisms of heat transport that involve vibrational modes with group velocity approaching zero.

While alloying and nano-inclusions are workable approaches, hierarchical grains introduce features that scale with size. Our findings support the interpretation of recent experiments, pinpointing the relevance of internal interfaces to scatter phonons with wavelengths that span over several length scales, towards the mesoscale effects on thermoelectrics.<sup>19</sup> In this work however, the chemistry was kept constant, *i.e.* only morphology changes were considered in PbSe, for a detailed analysis and understanding of the impact of grains.





## Conclusions

Grains are rather unwelcome in semiconductor technologies. In contrast, when it comes to suggesting a different perspective for improved thermoelectric performance, grains are superior phonon scatterers. In this work, by means of molecular dynamics techniques, we proposed an approach to systematically engineer hierarchical grains in B1 PbSe and we evaluated their impact on  $\kappa_l$ . Grains allow for a broader frequency range of phonon scattering, including frequencies below  $\sim 1$  THz, which are hardly attainable by any other nano-engineering approach. Furthermore, grains and grain boundaries are features that scale with size. Therefore, a larger, isotropic impact can be expected, as demonstrated in this work. Recent experiments show that ball-milled PbSe retains a high power factor.<sup>25</sup> In addition, it has been proposed that increased power factor may be achieved in polycrystalline materials through electron filtering at grain boundaries.<sup>3</sup> While we have concentrated our study on isolating grain effects as a result of purely structural features, additional ingredients can be added to further improve properties, like nano-inclusions within large grains, and alloying, locally or over the whole crystal. Furthermore, in coherently aligned grains like in Fig. 3 electrical properties can be expected to remain largely unaffected, therefore facilitating the preservation of a high overall electronic power factor in the presence of extended grain features. However, the study of the effect of grain boundaries on electronic transport in PbSe would deserve a separate study.

## Methods

### Transition path sampling molecular dynamics

Transition path sampling<sup>26</sup> molecular dynamics (TPS-MD) iterations within the NpT ensemble were implemented by applying momentum modifications on selected trajectory snapshots, keeping total energy, momentum, and angular momentum unchanged. Propagating the new configuration in both directions in time provides a new trajectory that is examined for the B1  $\rightarrow$  B2  $\rightarrow$  B1 process, respectively. Iterations are performed until trajectory convergence (characterised by stable mechanistic features) is reached. The simulation scheme requires a model trajectory connecting the limiting structures. Here, we have commenced the simulation from a path connecting B1 to B2, obtained from a geometric-topological approach, based on transforming minimal surfaces.<sup>40</sup> The classical MD simulations were carried out by using the DLPOLY package.<sup>49</sup> The Newton's equations of motion were integrated with the Velocity Verlet algorithm. The PbSe pair potential of Schapotschnikow *et al.* was used.<sup>41</sup> Periodic boundary conditions are applied. Particle-mesh Ewald summation was used for long-range electrostatics. A relatively small simulation time step of 0.10 fs was used to ensure a good time-reversibility. The Melchionna/Nose-Hoover algorithm<sup>50</sup> ensured constant pressure and temperature. As such, anisotropic shape changes of the simulation box were allowed.

Several simulations were performed in the range 9–16 GPa, at 300 K, with a box of 1980 PbSe pairs. At 300 K, the lattice constant of B1 PbSe amounted to 6.1 Å.<sup>41</sup> In the course of iterations, the collective characteristics of the geometric model disappeared, and a regime characterised by nucleation and growth set in. Additionally, an intermediate appeared in the converged regime, which was not apparent from the geometric model. More than 300 transition pathways were collected after trajectory convergence. Fig. 1 was produced based on a typical trajectory collected in the converged regime.

### Grain, grain boundaries and heat flux

The intermediate structure of Fig. 1b was iteratively relaxed using the conjugated gradient method ( $p = 1$  kbar,  $T = 0$  K). This unit of 3690 atoms of B33 structural characteristics, inherited from TPS-MD, served as the starting point for generating PbSe with grains. For each desired size, the unit was enlarged by periodic replicas. Magnification factors of  $2 \times 2 \times 2$ ,  $4 \times 4 \times 4$ ,  $6 \times 6 \times 6$  and  $12 \times 12 \times 12$  were chosen, corresponding to 31 680, 253 444, 855 360, 6 842 880 atom boxes, respectively. Each structure was propagated at  $p = 1$  kbar and  $T = 300$  K (NpT anisotropic ensemble) until the averaged structural parameters were stable. A typical run was at least 400 ps long, depending on the size. For every grain box size (up to 253 444 atoms), a corresponding MD of grain-free PbSe was also prepared, obtained by periodically replicating the unit cell. This was used to evaluate the influence of the finite box size on the value of  $\kappa_l$ , see below for details. MD calculations and heat flux calculations were performed with LAMMPS.<sup>51</sup> Interatomic potential, integration algorithm and time step were the same as for TPS calculations.

### Lattice thermal conductivity

The lattice thermal conductivity  $\kappa_l$  was calculated using the Green-Kubo relation based on the fluctuation-dissipation theorem:<sup>52</sup>  $\kappa_l = \frac{1}{k_b VT^2} \int_0^\infty \frac{\langle J(t) \cdot J(0) \rangle}{3} dt$ .  $k_b$  is the Boltzmann constant,  $V$  is the volume of the system,  $T$  is the temperature and  $\frac{\langle J(t) \cdot J(0) \rangle}{3}$  is the heat current autocorrelation function averaged over three directions. The heat current vector for a pair potential is defined as:<sup>53</sup>  $J = \sum_i^N \epsilon_i v_i + \frac{1}{2} \sum_{ij, i \neq j}^N (\mathbf{F}_{ij} \cdot v_i) \mathbf{r}_{ij}$ .  $\epsilon_i$  and  $v_i$  are the total energy and velocity associated with atom  $i$ , respectively. Vector  $\mathbf{r}_{ij}$  denotes interatomic distances between atoms  $i$  and  $j$ , and  $\mathbf{F}_{ij}$  interatomic forces.

Size-dependence effects were investigated. This is necessary as a small simulation box may affect the computed value of the thermal conductivity. For semiconductors this is of relevance as low frequency phonons may have long mean free paths. To correct for this effect, for B1 systems with grain features we considered  $2 \times 2 \times 2$  (32k atoms) and  $4 \times 4 \times 4$  (256 atoms) supercells, obtained by replicating the smallest grain system of 4k atoms. The  $\kappa_l$  difference between the  $2 \times 2 \times 2$  replica 32k atom system, and the 4k atom system amounted to



0.3 W mK<sup>-1</sup>, while between the 2 × 2 × 2 and the largest 256k atom system the difference was reduced to less than 0.03 W nK<sup>-1</sup>. Accordingly, κ<sub>1</sub> was rescaled for both the 4k and 32k atom systems to match the 256k system. Size effects were also considered for the bulk B1 phase: at 300 K the values of κ<sub>1</sub> were the same within error bars for all the 4k, 32k and 256k atom systems considered. This shows how size effects in equilibrium MD simulations are not related to long mean free paths but rather to sampling sufficiently low frequency phonons, which usually have a wavelength shorter than the relevant mean free paths. For anisotropic systems containing grains, κ<sub>1</sub> was resolved for each Cartesian component.

### Group velocities and lifetimes

The dynamical matrix Ω was obtained in lattice dynamic calculations, computing derivatives of forces acting on atoms as finite differences. The matrix was computed and diagonalized in order to obtain eigenvectors *e* and eigenvalues ω<sup>2</sup> at the Γ-point ( $\vec{q} = 0$ ) of the Brillouin zone relative to the supercells.

Since the group velocities,  $\vec{v}_g = d\omega/d\vec{q}$ , at the Γ-point of a supercell are exactly zero, except for the 3 acoustic branches, there is no general consensus on how to evaluate the group velocities of non-periodic systems, and several effective approaches have been tested for amorphous systems or alloys.<sup>45,54,55</sup> Here we exploit the fact that periodic boundary conditions are applied, and we calculate  $d\omega(\vec{q})/d\vec{q}$  for a set of *q*-points on a 2 × 2 × 2 shifted Monkhorst–Pack mesh. We then define effective group velocities as a function of the frequencies,  $\vec{v}_g(\omega)$ , as the average of  $d\omega/d\vec{q}$  over a range between ω − δω and ω + δω with δω = 0.006 THz.

From the normalized autocorrelation function of the energies of each eigenmode lifetimes were calculated:

$$\tau_i = \int_0^\infty \frac{\langle E_i(\vec{q}, t) E_i(\vec{q}, 0) \rangle}{\langle E_i(\vec{q}, 0) E_i(\vec{q}, 0) \rangle} dt, \quad \text{where} \quad E_i(\vec{q}, t) = \frac{\omega_i^2 S_i^* S_i(\vec{q}, t)}{2} + \frac{S_i^* S_i(\vec{q}, t)}{2}, \quad \text{and} \quad S_i(\vec{q}, t) = \sqrt{N} \sum_j \sqrt{M_j} e^{(-i\vec{q} \cdot \vec{r}_j)} e_i^*(\vec{q}) \cdot u_j(t).$$

*S'* is the derivative of *S*, and *u<sub>j</sub>* is the displacement of atom *j* in MD trajectories. Once all these contributions are available, further calculations of the effective mean free path (MFP) are straightforward.<sup>45</sup> For a certain mode *i*, the MFP is given by λ<sub>*i*</sub> = ν<sub>*i*</sub>τ<sub>*i*</sub>.

### Fourier analysis

All three systems containing grains (Fig. 5) were Fourier transformed, considering Pb atoms only. Structure factors *F<sub>hkl</sub>* were

$$\text{evaluated according to the formula: } F_{hkl} = \sum_{i=1}^N f_i \exp(2\pi i \vec{h} \cdot \vec{r}_i) = A_{hkl} + iB_{hkl}, \quad A_{hkl} = \sum_{i=1}^N f_i \cos(2\pi i \vec{h} \cdot \vec{r}_i), \quad B_{hkl} = \sum_{i=1}^N f_i \sin(2\pi i \vec{h} \cdot \vec{r}_i).$$

Therein,  $\vec{h} = (hkl)$  is a reciprocal space vector and  $\vec{r}_i$  is a coordinate of a crystal structure of *N* atoms. The peak intensity for a *hkl* index is calculated as the modulus of the vector,

$\|F_{hkl}\| = \sqrt{(A_{hkl})^2 + (B_{hkl})^2}$ . The factor *f<sub>i</sub>* accounts for the scattering due to electrons. Since the value distribution of *F<sub>hkl</sub>* depends on the crystal structure, delta functions centred on

each atom were used. *hkl* Values were chosen in the range −40 ≤ *h, k, l* ≤ 40. This choice ensures that the highest peak intensities are accounted for.

## Acknowledgements

D. S. and S. L. thank the DFG for support under the priority project SPP 1415, as well as ZIH Dresden for the generous allocation of computational resources. S. L. thanks the DFG for support in the form of a Heisenberg Fellowship. Via our membership of the UK's HPC Materials Chemistry Consortium, which is funded by EPSRC (EP/L000202), this work made use of the facilities of ARCHER, the UK's National High-Performance Computing Service, which is funded by the Office of Science and Technology through EPSRC's High End Computing Programme. We thank Dr Min Gao, Cardiff for insightful discussions. We are thankful to Samuel Jobbins for critically reading the manuscript.

## References

- G. J. Snyder and E. S. Toberer, *Nat. Mater.*, 2008, **7**, 105.
- G. Chen, M. S. Dresselhaus, G. Dresselhaus, J. P. Fleurial and T. Caillat, *Int. Mater. Rev.*, 2003, **48**, 45–66.
- J. R. Sootsman, D.-Y. Chung and M. G. Kanatzidis, *Angew. Chem., Int. Ed. Engl.*, 2009, **48**, 8616–8639.
- D. M. Rowe, *Handbook of Thermoelectrics: Macro to Nano*, CRC Press, Boca Raton, 2005.
- M. Zebarjadi, K. Esfarjani, M. S. Dresselhaus, Z. F. Ren and G. Chen, *Energy Environ. Sci.*, 2012, **5**, 5147–5162.
- K. Biswas, J. He, Q. Zhang, G. Wang, C. Uher, V. P. Dravid and M. G. Kanatzidis, *Nat. Chem.*, 2011, **3**, 160.
- T. C. Harman, P. J. Taylor, M. P. Walsh and B. E. LaForge, *Science*, 2002, **297**, 2229.
- J. He, L.-D. Zhao, J.-C. Zheng, J. W. Doak, H. Wu, H.-Q. Wang, Y. Lee, C. Wolverton, M. G. Kanatzidis and V. P. Dravid, *J. Am. Chem. Soc.*, 2013, **135**, 4624.
- H. Wang, Y. Pei, A. D. LaLonde and G. J. Snyder, *Adv. Mater.*, 2011, **23**, 1366–1370.
- J. Androulakis, C. Lin, H. Kong, C. Uher, C. Wu, T. Hogan, B. A. Cook, T. Caillat, K. M. Paraskevopoulos and M. G. Kanatzidis, *J. Am. Chem. Soc.*, 2007, **129**, 9780.
- P. F. P. Poudeu, J. D'Angelo, H. Kong, A. Downey, J. L. Short, R. Pcionek, T. P. Hogan, C. Uher and M. G. Kanatzidis, *J. Am. Chem. Soc.*, 2006, **128**, 14347.
- Z. Wang, J. E. Alaniz, W. Jang, J. E. Garay and C. Dames, *Nano Lett.*, 2011, **11**, 2206–2213.
- C. Hua and A. J. Minnich, *Semicond. Sci. Technol.*, 2014, **29**, 124004.
- C. Melis and L. Colombo, *Phys. Rev. Lett.*, 2014, **112**, 065901.
- K. T. Regner, D. P. Sellan, Z. Su, C. H. Amon, A. J. H. McGaughey and J. A. Malen, *Nat. Commun.*, 2013, **4**, 1640.



- 16 Y. He, D. Donadio and G. Galli, *Nano Lett.*, 2011, **11**, 3608–3611.
- 17 J. Garg, N. Bonini, B. Kozinsky and N. Marzari, *Phys. Rev. Lett.*, 2011, **106**, 045901.
- 18 Z. T. Tian, J. Garg, K. Esfarjani, T. Shinga, J. Shiomi and G. Chen, *Phys. Rev. B: Condens. Matter*, 2012, **85**, 184303.
- 19 K. Biswas, J. He, I. D. Blum, C.-I. Wu, T. P. Hogan, D. N. Seidman, V. P. Dravid and M. G. Kanatzidis, *Nature*, 2012, **489**, 414.
- 20 L. D. Zhao, H. J. Wu, S. Q. Hao, C. I. Wu, X. Y. Zhou, K. Biswas, J. Q. He, T. P. Hogan, C. Uher, C. Wolverton, V. P. Dravid and M. G. Kanatzidis, *Energy Environ. Sci.*, 2013, **6**, 3346–3355.
- 21 D. Wolf, V. Yamakov, S. R. Phillpot, A. Mukherjee and H. Gleiter, *Acta Mater.*, 2005, **53**, 1–40.
- 22 A. Bodapati, P. K. Schelling, S. R. Phillpot and P. Keblinski, *Phys. Rev. B: Condens. Matter*, 2006, **74**, 245207.
- 23 P. Keblinski, S. R. Phillpot, D. Wolf and H. Gleiter, *Acta Mater.*, 1997, **45**, 987–998.
- 24 J. He, M. G. Kanatzidis and V. P. Dravid, *Mater. Today*, 2013, **16**, 166–176.
- 25 Q. Zhang, H. Wang, W. Liu, H. Wang, B. Yu, Q. Zhang, Z. Tian, G. Ni, S. Lee, K. Esfarjani, G. Chen and Z. Ren, *Energy Environ. Sci.*, 2012, **5**, 5246–5251.
- 26 P. G. Bolhuis, D. Chandler, C. Dellago and P. L. Geissler, *Annu. Rev. Phys. Chem.*, 2002, **53**, 291.
- 27 S. Leoni, R. Ramlau, K. Meier, M. Schmidt and U. Schwarz, *Proc. Natl. Acad. Sci. U. S. A.*, 2008, **105**, 19612.
- 28 F. Demiray and S. Berber, *Phys. Scr.*, 2013, **88**, 015603.
- 29 R. Zwanzig, *Annu. Rev. Phys. Chem.*, 1965, **16**, 67.
- 30 T. Chattopadhyay, A. Werner and H. G. von Schnering, *Rev. Phys. Appl.*, 1984, **19**, 807.
- 31 S. V. Ovsyannikov, V. V. Shchennikov, A. Y. Manakov, A. Y. Likhacheva, Y. S. Ponosov, V. E. Mogilenskikh, A. P. Vokhmyanin, A. I. Ancharov and E. P. Skipetrov, *Phys. Status Solidi B*, 2009, **246**, 615.
- 32 M. Baleva, E. Mateeva and E. P. Trifonova, *J. Mater. Sci.*, 1999, **34**, 795–799.
- 33 R. Ahuja, *Phys. Status Solidi B*, 2003, **235**, 341–347.
- 34 H. T. Stokes, D. M. Hatch, J. J. Dong and J. P. Lewis, *Phys. Rev. B: Condens. Matter*, 2004, **69**, 174111.
- 35 R. Martoňák, A. Laio and M. Parrinello, *Phys. Rev. Lett.*, 2003, **90**, 075503.
- 36 R. Martoňák, D. Donadio, A. R. Oganov and M. Parrinello, *Nat. Mater.*, 2006, **5**, 623.
- 37 D. Zahn and S. Leoni, *Phys. Rev. Lett.*, 2004, **92**, 250201.
- 38 S. Leoni and S. E. Boulfelfel, *Modern Methods of Crystal Structure Prediction*, ed. A. R. Oganov, Wiley-VCH, Berlin, 2011, pp. 181–221.
- 39 S. Leoni, *Chem. – Eur. J.*, 2007, **13**, 10022.
- 40 S. Leoni and D. Zahn, *Z. Kristallogr.*, 2004, **219**, 339.
- 41 P. Schapotschnikow, M. A. van Huis, H. W. Zandbergen, D. Vanmaekelbergh and T. J. H. Vlugt, *Nano Lett.*, 2010, **10**, 3966.
- 42 V. A. Blatov, *IUCr CompComm Newsletter*, 2006, **7**, 4.
- 43 K. S. Upadhyaya, M. Yadav and G. K. Upadhyaya, *Phys. Status Solidi B*, 2002, **229**, 1129–1138.
- 44 J. Androulakis, D.-Y. Chung, X. Su, L. Zhang, C. Uher, T. C. Hasapis, E. Hatzikraniotis, K. M. Paraskevopoulos and M. G. Kanatzidis, *Phys. Rev. B: Condens. Matter*, 2011, **84**, 155207.
- 45 Y. He, D. Donadio, J.-H. Lee, J. C. Grossman and G. Galli, *ACS Nano*, 2011, **5**, 1839.
- 46 J. Garg, N. Bonini and N. Marzari, *Nano Lett.*, 2011, **11**, 5135–5141.
- 47 P. B. Allen and J. L. Feldman, *Phys. Rev. B: Condens. Matter*, 1993, **48**, 12581–12588.
- 48 Y. He, D. Donadio and G. Galli, *Appl. Phys. Lett.*, 2011, **98**, 144101.
- 49 W. Smith and T. R. Forester, *J. Mol. Graphics*, 1996, **14**, 136.
- 50 S. Melchionna, G. Ciccotti and B. L. Holian, *Mol. Phys.*, 1993, **78**, 533.
- 51 S. J. Plimpton, *J. Comp. Physiol.*, 1995, **117**, 1.
- 52 D. A. McQuarrie, *Statistical Mechanics*, University Science Books, Sausalito, CA, 2000, p. 642.
- 53 G. Green, Y. Cho, J. Hartnett and A. Bar-Cohen, *Advances in Heat Transfer*, Elsevier, New York, 2006, p. 212.
- 54 J. M. Larkin and A. J. H. McGaughey, *J. Appl. Phys.*, 2013, **114**, 023507.
- 55 J. M. Larkin and A. J. H. McGaughey, *Phys. Rev. B: Condens. Matter*, 2014, **89**, 144303.

